Optics Letters

Far-field super-focusing by a feedback-based wavefront shaping method

ZhengDong Gao,[1,2,†] YanQi Qiao,[1,2,†] Lanting Li,[1,2] and XianFeng Chen[1,2,*]

[1]State Key Laboratory of Advanced Optical Communication Systems and Networks School of Physics and Astronomy, Shanghai Jiao Tong University, Shanghai 200240, China
[2]Key Laboratory for Laser Plasma (Ministry of Education), Collaborative Innovation Center of IFSA (CICIFSA), Shanghai Jiao Tong University, Shanghai 200240, China
*Corresponding author: xfchen@sjtu.edu.cn

Received 3 January 2019; accepted 19 January 2019; posted 25 January 2019 (Doc. ID 356736); published 14 February 2019

Abbe diffraction limit has always been an important subject in conventional far-field focusing and imaging systems, where the resolution of an image is usually limited to 0.5λ/NA. Recently, the studies of the optical super-oscillation lens (SOL) enable us to break the limitation in both theory and practice successfully. Here a genetic algorithm was introduced to design the SOL phase more controllably and precisely obtain much better focusing such as the focal spot with 0.105λ/NA (or 79.0% minification) in the simulation and 65.5% minification in the experimental demonstration. This technique is of great significance in advanced optical lithography or biology microscopy, because it promises non-invasive unlabelled imaging from the far field.

https://doi.org/10.1364/OL.44.001035

In most cases, the resolution of far-field imaging is determined by the wavelength λ of the illuminating light due to the diffraction limit [1]. Theoretically, the width of a focal spot is calculated by the formula $\Delta x = 0.5\lambda/\mathrm{NA}$, where NA is the effective numerical aperture of the imaging system [2]. Generally, the best achievable resolution is around 200 nm for visible light, which makes far-field imaging limited in nanotechnology such as microscopy and optical lithography. Therefore, it is always significant to find a way to break the Abbe diffraction limit in far-field focusing and imaging. In the past few decades, several valid techniques have been developed such as near-field imaging based on detecting an evanescent-wave [3–7] and the imaging requiring fluorescent labeling [8–12]. However, these kinds of methods are not usually easy to be applied because of the stringent proximity restrictions and heavy needs for pre-labeling [13]. Other previous research has found that a super-oscillation lens (SOL) could make far-field super-resolution possible by modulating the amplitude and phase of incident light periodically [13–17]. Usually, a lot of parameters need to be figured out to design a suitable SOL [18,19], which was a troublesome process and needed a great amount of calculation.

In computer science and operation research, the genetic algorithm (GA) was commonly used to generate high-quality solutions for optimization by relying on bio-inspired operators such as mutation, crossover, and selection. In this Letter, we broke the diffraction limit by a feedback-based wavefront phase-shaping method [20], as the SOL suggested. The efficient GA enabled us to find the optimal results in such a complex situation in relatively short time. We observed ideal shrink effects of focal spots such as 0.105λ/NA (or 79.0% minification) in the simulation and 65.5% minification in the experimental demonstration. According to the simulation, the width of the focal spots could be only dozens of nanometers. Besides, a GA-designed SOL is very easy to fabricate, controllable for various applications and robust to the complex environments. Hence, this technique provides a possible way to make progress in these applications.

According to the Fresnel–Kirchhoff diffraction theory, the conventional image function is calculated by the Fraunhofer diffraction formula [21]:

$$\tilde{U}(P) = C \iint_{00}^{R2\pi} e^{-ik\rho w\cos(\varphi-\theta)}\rho \mathrm{d}\rho\mathrm{d}\varphi, \tag{1}$$

where (ρ, φ) is the polar coordinates of a typical point in the aperture, and (w, θ) is the coordinate of the point P in the diffraction pattern. The amplitude distributions of the focal spot with a SOL can be expressed as

$$\tilde{U}(P) = C \iint_{00}^{R2\pi} e^{-ik\rho w\cos(\varphi-\theta)} e^{i\psi(\rho,\varphi)}\rho \mathrm{d}\rho\mathrm{d}\varphi, \tag{2}$$

where $e^{i\psi(\rho,\varphi)}$ is phase shaping due to the phase mask in a SOL.

A simple phase mask was designed as a 1-D modulation mask, where the phases were discrete radial variable in polar coordinate. Therefore, the additional item $e^{i\psi(\rho,\varphi)}$ in the Fraunhofer diffraction formula could be simplified as $e^{i\psi(\rho)}$. Different phases were distributed like rings with the same width, as shown in Fig. 1(a). Each concentric ring was linked to a specific gray value ranging from 0 to 2π with the interval of 0.01. The mask provided a phase type modulation of the incident light, and the modified light was focused by a normal lens afterward, as shown in Fig. 1(b).

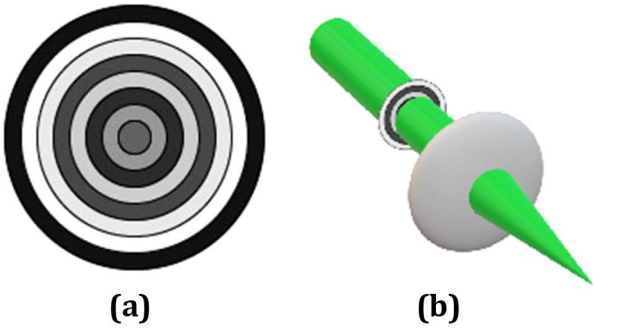

Fig. 1. (a) Phase mask, eight rings. The gray value represents specific phase shaping ranging from 0 to 2π with the interval of 0.01. (b) Diagrammatic sketch of the process of super-focusing with a phase mask.

Sacrificing central focal intensity (CFI) is indispensable when a SOL is used [13,18]. In this Letter, different CFIs were preserved to obtain a different focusing quality, which was defined as CFI $= \frac{I_s(0,0)}{I_o(0,0)}$, where $I_s(0,0)$ was the intensity of the (0,0) coordinate on the focal plane under SOL masks, and $I_o(0,0)$ was the intensity without phase masks. Here the parameter CFI was fixed to be 0.1%, 1%, and 10%. The focusing efficiency of energy (FEE) was also defined to present the energy ration in the super-oscillatory focal spot. The full width at half-maximum (FWHM) was applied to define the size of the focal spot. The shrink factor η was calculated at the same time to illustrate the optimization efficiency, which equaled the ratio of the decrease of FWHM to the original FWHM. The simulation to realize the process of GA included selection, crossover, and mutation [20]. The latter generation would generally do better than the former, which indicated an optimization process.

The iteration number of the process was set as 1000 during the simulation. The phase masks with different numbers of rings (20 or 40) were applied. We generally set the size of the field of view on the image plane to be $2\lambda/\mathrm{NA}$. Some typical simulation results were shown in Table 1 and Fig. 2.

It is clear that the focal spots became dimmer and smaller with the decrease of the CFI, as shown in Table 1. For the mask with 20 rings, the FWHM decreased from 0.300 to $0.130\lambda/\mathrm{NA}$ with the CFI decreasing from 10% to 0.1%. For the mask with 40 rings, the FWHM decreased similarly from 0.274 to $0.105\lambda/\mathrm{NA}$, as expected. Furthermore, with the phase modulation becoming finer, which means the number of rings increased, the focal spots could get smaller after optimizations. For example, the FWHM decreased from 0.130 to $0.105\lambda/\mathrm{NA}$ with a fixed CFI of 0.1%.

Table 1. Parameters of Focal Spots After Optimization

Rings	CFI	FEE	FWHM (λ/NA)	Shrink η
20	0.1%	1.25×10^{-4}	0.130	74.0%
20	1%	3.71×10^{-3}	0.209	58.2%
20	10%	0.061	0.300	40.0%
40	0.1%	1.01×10^{-4}	0.105	79.0%
40	1%	2.72×10^{-3}	0.170	66.0%
40	10%	0.054	0.274	45.2%

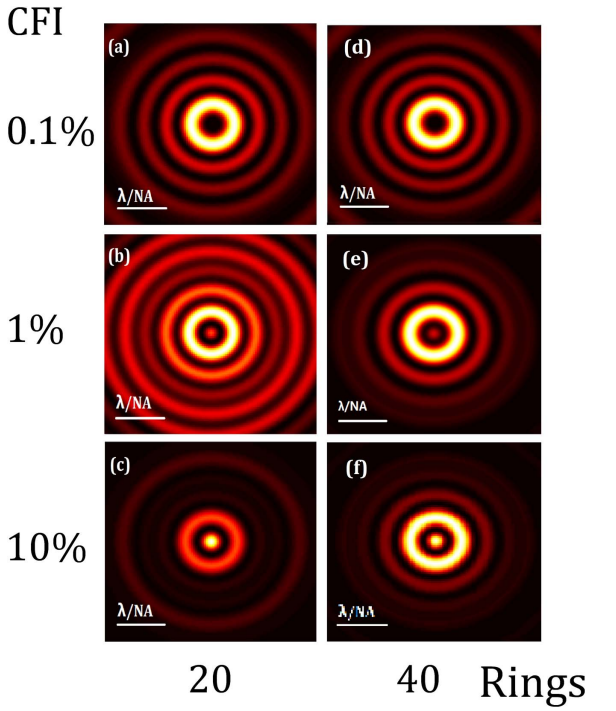

Fig. 2. Intensity distribution of super-focusing under different masks. (a)–(c) 20-ring mask, focal spot preserves 0.1%, 1%, and 10% intensity, respectively; (d)–(f) 40-ring mask, focal spot preserves 0.1%, 1%, and 10% intensity, respectively.

It is worth mentioning that even though we achieved focal spots with widths $0.105\lambda/\mathrm{NA}$, the trade-off of sacrificing central intensity was so much that the focal spots were hardly seen compared to the sidebands [Figs. 2(a) and 2(d)]. Under this circumstance, the influence of sidebands needed to be eliminated for further applications.

Theoretically, there is no limitation value of the minification, since we could always decrease CFI to obtain a smaller spot until the CFI becomes zero.

The experimental demonstration based on GA was also realized in this Letter. The setup is illustrated in Fig. 3. The light source was a continuous-wave laser at the wavelength of 532 nm (MGL-III-532nm-50mW-18111845). A half-wave plate and a Glan–Taylor polarizer were used for polarization and power control. Phase-shaping masks were applied by a spatial light modulator (SLM). The SLM had a resolution of 1920×1080 pixels, each with a rectangular area of

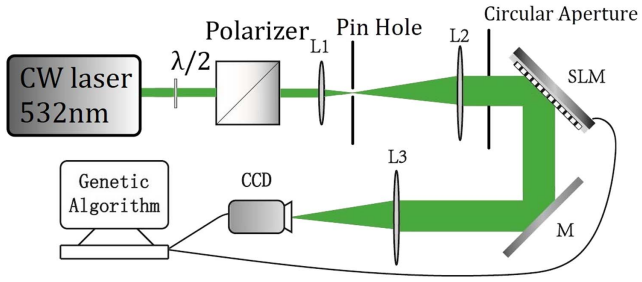

Fig. 3. Experimental setup for a SOL. $\lambda/2$, half-wave plate; L_{123}, lens; $f_{123} = 50$, 500, and 1100 mm, respectively; M, mirror; SLM, spatial light modulator; diameter of circular aperture $d = 5$ mm.

9.26 μm × 9.26 μm. The focal spot was imaged on a multispectral two-channel charge-coupled device (CCD) camera (MER-131-210U3MC) connected with the computer. The CCD camera had a resolution of 1280 × 1024 pixels, each with a rectangular area of 4.65 μm × 4.65 μm. We particularly used a small NA (2.27×10^{-3}) imaging system and a beam expansion system to make the focal spot suitable for CCD detection.

The FWHM of the spot captured by the CCD was recorded and served as a feedback to optimize the SLM phase mask. A GA was applied to realize the optimization for its robustness to the noisy environments [20]. Typically, the 40-ring mask was applied in the experimental demonstration, since it was expected to bring us a better focusing result compared to the 20-ring mask, according to the simulation. It is worth mentioning that the width of each ring was much larger than the wavelength of the incident light so that the additional diffraction was negligible. The original focal spot with a normal lens s shown in Fig. 4(b). Accordingly, the intensity-radius (parallel to x axis) graphs are obtained [Fig. 4(a)]. In the theoretical analysis, $\lambda = 532$ nm, and NA $= 2.27 \times 10^{-3}$, which gave a diffraction limited spot size of 117.0 μm. In reality, the focal spot had a slightly larger width of 134.9 ± 4 μm under the experimental setup, which is acceptable and similar to some previous works on super-focusing [22].

At the first of the optimization, random phase masks were applied to reshape the wavefront of the incident light. The central focal spot intensity at one single CCD pixel was recorded and fixed to preserve 1% or 10% intensity (CFI ∼ 1%, CFI ∼ 10%). After several iterations of the GA, the focal spots with a much smaller width were obtained. The Intensity-radius (parallel to x axis) graphs and the optimized focal spot images were shown in Fig. 5. Accordingly, the final optimized FWHM were estimated to be 46.5 and 74.6 μm, under the different conditions where the CFI was 1% and 10%, respectively.

The shrink factor η was detected with the iteration number during the optimization. As expected, η increased generally with the generation number until saturation. Typical η in our experiment was estimated to be 65.5% and 44.7% with different CFIs after nearly 300 generations. A summary of the experimental results is shown in Table 2.

When the CFI was 1%, FWHM of the optimized focal spot was 46.5 μm, according to our experimental results. As for the simulation results, the FWHM of the optimized focal spots was 39.8 μm (0.170λ/NA) under the same focusing condition ($\lambda = 532$ nm, NA $= 2.27 \times 10^{-3}$, CFI ∼ 1%, 40 rings). Basically, these two foci were comparable, and the deviation

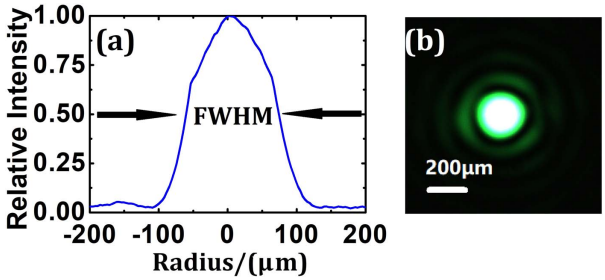

Fig. 4. (a) Light intensity distribution and FWHM of the original focal spot without a phase mask and (b) image of original focal spot without phase masks.

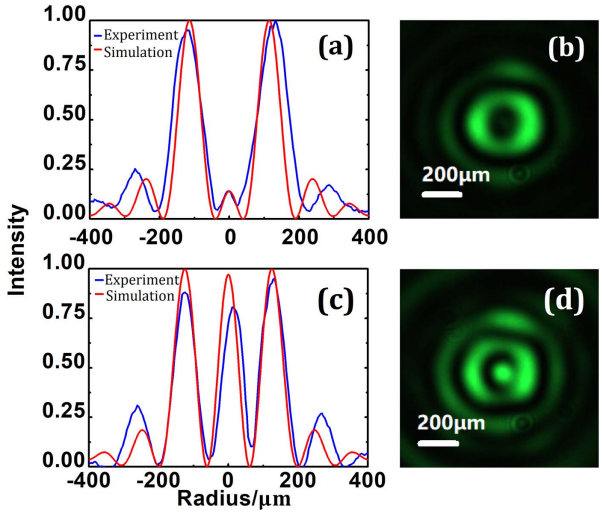

Fig. 5. Theoretical (red) and experimental (blue) light intensity distribution of the focal spot under a 40-ring phase mask with different CFIs. The light intensity was normalized. (a) and (b) CFI was fixed to be 1%; (c) and (d) CFI was fixed to be 10%.

between them was acceptable [Fig. 5(a)]. Besides, as expected, the first-order sideband was much brighter than the focal spot as shown in Fig. 5(b). The focal plane images shown in Figs. 5(b) and 2(e) were almost identical, indicating that the experimental results were in good agreement with the theoretical studies.

When the CFI was 10%, the experimental results were as good as the simulation claiming, too, as shown in Fig. 5(c). The theoretical FWHM of the optimized focal spot was 64.1 μm (0.274λ/NA) and the detected FWHM was 74.6 μm under the experimental setup. The sidebands also coincided with the theoretical results [Figs. 5(d) and 2(f)]. The location, width, and light intensity of the first-order sideband were all in agreement with the simulation results, which strongly prove the validity of the theoretical designs.

Under this circumstance, other promising experimental focusing results could be expected when we fix different CFIs. However, due to a lack of detectors with high resolution and sensibility, it was temporarily hard to accomplish the experiment with the CFI below 1%.

Furthermore, when a 40-ringsmask was applied, the shrink factor η was 65.5% or 44.7% with fixed CFIs of 1% or 10%, respectively, in the experiments. The relative values of η were 66.0% and 45.2%, respectively, in the simulation. The best simulation result of 79.0% with a fixed CFI of 0.1% was not obtained in experiments due to the experimental deficiencies discussed above, including the limitation of detecting precision and the drawback that the GA cannot get a global maximum.

Table 2. Parameters of Focal Spots

Mask	CFI	FWHM (μm)	Theoretical FWHM (μm)	Shrink η
Origin	/	134.9	117.0	/
Mask	1%	46.5	39.8	65.5%
Mask	10%	74.6	64.1	44.7%

It is worth mentioning that the goal of our experiments was to demonstrate that the focal spot could be shrunk at the theoretical minification and break the Abbe diffraction limit. Therefore, a small NA was used in the experimental setup to make the focal spot discernible. We did not try to obtain a much smaller focal spot whose width was a few tens of nanometer with a larger NA. However, there is every reason to believe that one could expect such a smaller focal spot for further study, once the experimental setup with a large NA approaching 1 was applied.

In conclusion, inspired by the previous studies of a SOL, we introduced the GA and designed a phase modulation to make further development of the study. With the decrease of the CFI and adding radial variables of phase masks, the focal spots could get much smaller. The smallest FWHM of the focal spots we achieved was only $0.105\lambda/\mathrm{NA}$ (or 79.0% minification), which meant that the width of focal spots could be only dozens of nanometers. In experiments a focal spot with 46.5 μm FWHM was obtained (65.5% minification). As discussed above, better results could be expected through overcoming the drawbacks of the limitation of detecting precision and achieving an optimal algorithm. For example, we could realize the simulation results when the CFI was under 1% with the help of a more acute and sensitive detector. Then a perfect focal spot with several or tens of nanometer width could be expected.

Besides, there are some other prospective works for future study. Other optical parameters such as polarization and amplitude could be added into the feedback-based wavefront shaping. Theoretically, it is possible to obtain a better superfocusing result from the far field with multiple modulations of wavefront, which means that the feedback-based wavefront shaping method has a promising application in far-field superfocusing and imaging, especially for the systems with random interferences and inevitable deficiencies.

Funding. National Key R&D Program of China (2017YFA0303701, 2018YFA0306301); National Natural Science Foundation of China (NSFC) (11734011); Foundation for the Development of Science and Technology Museums in China (17JC1400400).

†These authors contributed equally to this Letter.

REFERENCES

1. Rayleigh, Philos. Mag. **42**, 167 (1896).
2. E. Abbé, Arch. Mikrosk. Anat. **9**, 413 (1873).
3. E. H. Synge, Philos. Mag. **6**, 356 (1928).
4. D. W. Pohl, W. Denk, and M. Lanz, Appl. Phys. Lett. **44**, 651 (1984).
5. J. B. Pendry, Phys. Rev. Lett. **85**, 3966 (2000).
6. Z. Jacob, L. V. Alekseyev, and E. Narimanov, Opt. Express **14**, 8247 (2006).
7. L. Markley, A. M. H. Wong, Y. Wang, and G. V. Eleftheriades, Phys. Rev. Lett. **101**, 113901 (2008).
8. S. Nie and S. R. Emory, Science **275**, 1102 (1997).
9. S. W. Hell and J. Wichmann, Opt. Lett. **19**, 780 (1994).
10. M. J. Rust, M. Bates, and X. Zhuang, Nat. Methods **3**, 793 (2006).
11. E. Betzig, G. H. Patterson, R. Sougrat, O. W. Lindwasser, S. Olenych, J. S. Bonifacino, M. W. Davidson, J. Lippincott-Schwartz, and H. F. Hess, Science **313**, 1642 (2006).
12. A. Szameit, Y. Shechtman, E. Osherovich, E. Bullkich, P. Sidorenko, H. Dana, S. Steiner, E. B. Kley, S. Gazit, T. Cohen-Hyams, S. Shoham, M. Zibulevsky, I. Yavneh, Y. C. Eldar, O. Cohen, and M. Segev, Nat. Mater. **11**, 455 (2012).
13. X. Dong, A. M. H. Wong, M. Kim, and G. V. Eleftheriades, Optica **4**, 1126 (2017).
14. H. Liu, Y. Yan, and G. Jin, Appl. Opt. **45**, 95 (2006).
15. N. Bokor and Y. Iketaki, Appl. Spectrosc. **68**, 353 (2014).
16. M. V. Berry and S. Popescu, J. Phys.A **39**, 6965 (2006).
17. F. Huang, N. Zheludev, Y. Chen, and F. J. G. De Abajo, Appl. Phys. Lett. **90**, 091119 (2007).
18. K. S. Rogers, K. N. Bourdakos, G. Yuan, S. Mahajan, and E. T. F. Rogers, Opt. Express **26**, 8095 (2018).
19. Z. Wen, Y. He, Y. Li, L. Chen, and G. Chen, Opt. Express **22**, 22163 (2014).
20. Y. Qiao, Y. Peng, Y. Zheng, F. Ye, and X. Chen, Opt. Lett. **42**, 1895 (2017).
21. M. Born and E. Wolf, *Principles of Optics*, 7th ed. (Cambridge University, 2013).
22. I. M. Vellekoop, A. Lagendijk, and A. P. Mosk, Nat. Photonics **4**, 320 (2010).